Eur. Phys. J. D **6**, 355-364 (1999)

THE EUROPEAN PHYSICAL JOURNAL D

EDP Sciences

Imaging and tunneling spectroscopy of gold nanocrystals and nanocrystal arrays

T.P. Bigioni[1], L.E. Harrell[2,3,a], W.G. Cullen[2,3], D.K. Guthrie[3,4], R.L. Whetten[1,2,3], and P.N. First[2,3,b]

[1] School of Chemistry, Georgia Institute of Technology, Atlanta, GA 30332-0400, USA
[2] School of Physics, Georgia Institute of Technology, Atlanta, GA 30332-0430, USA
[3] Microelectronics Research Center, Georgia Institute of Technology, Atlanta, GA 30332-0269, USA
[4] School of Electrical and Computer Engineering, Georgia Institute of Technology, Atlanta, GA 30332-0250, USA

Received: 10 September 1998 / Received in final form: 16 February 1999

Abstract. Scanning tunneling microscopy (STM) and spectroscopy (STS) have been used to determine the structural and electronic properties of thiol-passivated 29000 amu gold nanocrystals, both individually and in spontaneously formed quasi-two-dimensional arrays. Experiments were performed at temperatures of 300 K, 77 K, and 8 K. Even at room temperature, tunneling through these 1.7 nm nanocrystals is shown to give rise to a Coulomb blockade. At cryogenic temperatures, the spectroscopy of the nanocrystals in arrays and in isolation shows an incremental charging effect (the Coulomb staircase) and evidence is found for quantization of the electronic states.

PACS. 61.46.+w Clusters, nanoparticles, and nanocrystalline materials – 71.24.+q Electronic structure of clusters and nanoparticles – 73.61.Tm Nanocrystalline materials

1 Introduction

Nanometer-scale clusters of materials have demonstrated great potential for a variety of applicatons ranging from catalysts [1,2] to novel optoelectronic [3] and electronic [4] devices. Nanometer crystallites (nanocrystals) are also interesting because their properties may be dominated by electron correlations that are often ignored in the bulk material. Metal clusters in particular must be understood from a scale at which their properties are best described by an itinerant electron picture down to sizes where a molecular orbital approach is more appropriate.

Metal nanocrystals, passivated by an adsorbed monolayer, represent the transitional regime between the bulk metal and metal-cluster compounds, where bulk properties of the material begin to change due to finite-size effects [8,9]. Typical passivated metal nanocrystals investigated include Au [10–12], Ag [13,14] and Pt [15–17]. They are generally passivated with a layer of organic adsorbates that serves to stabilize the cores by protecting them from aggregation and sintering.

It has been shown that passivated Au nanocrystals have crystalline cores that come in preferred sizes [10]. The discretization of possible core sizes is due to the energetics of both surface faceting for a finite crystal and the distribution of electronic states. This effect is strongest for the smallest core sizes where both electronic and atomic shell closings produce the most pronounced thermodynamic minima. In the size range 1-2 nm diameter, a family of stable nanocrystals has been found with crystalline Au cores consisting of up to ~ 250 Au atoms, the surfaces of which are passivated by a monolayer of alkane thiols [8]. Members of this family have been studied using a number of techniques including mass spectrometry [18], powder X-ray diffraction (XRD) [8], optical absorption spectroscopy [9], electrochemical voltammetry [19,20] and nuclear magnetic resonance [21].

A major goal of our ongoing work to fully characterize these new materials is to measure nanocrystal electronic structures in order to determine the factors that govern their stability. This paper presents initial results of these investigations by scanning tunneling microscopy (STM) and spectroscopy (STS) on the 29000 amu (29k) thiol-passivated Au nanocrystal, which is currently the most highly characterized member of the aforementioned family. These nanocrystals have a mean core diameter of 1.7 nm [21] and their mass is known to ± 2000 amu [18].

Figure 1(a) shows the idealized geometry of the experiments described in this work. It is similar to other tunneling experiments on passivated [22] and unpassivated [23,24] nanocrystals, and the results also relate to single-nanoparticle tunneling experiments employing microfabricated junctions [25–28]. As demonstrated by these and other experiments, a universal feature of tunneling current *versus* voltage (I-V) spectra from such small metal

[a] *Present address*: Physics Dept., U.S. Military Academy, West Point, NY 10996, USA
[b] e-mail: `first@physics.gatech.edu`

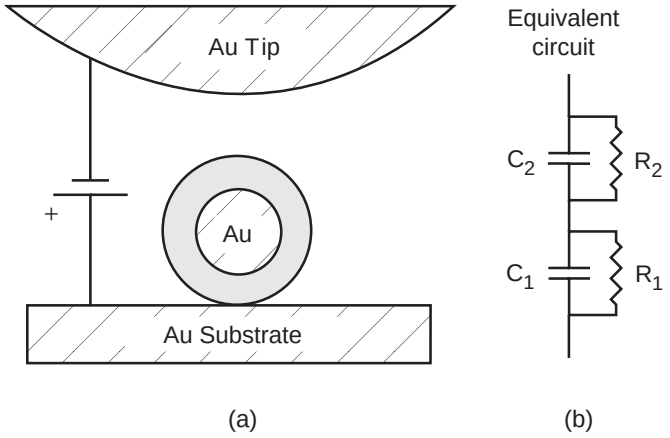

Fig. 1. (a) Schematic of the STM experimental geometry. The shaded ring represents the adsorbed dodecanethiol monolayer. (b) Equivalent circuit used as a basis for modeling the current-voltage characteristics of the experimental system.

particles is Coulomb charging [7], which serves to complicate density-of-states measurements. For macroscopic electrodes, tunneling I-V (or $\mathrm{d}I/\mathrm{d}V$) functions are closely related to the one-electron density of states in the electrodes. By contrast, for submicron- to nanometer-scale particles the electron addition energy may be dominated by Coulomb correlations and cannot be associated directly with the one-electron energy spectrum of the neutral cluster. However, when the wave functions of the particle are delocalized, excess charge always lies near the surface, and the dominant Coulomb correlations can be treated as a classical charging energy e^2/C, where C is a constant effective capacitance for the particle. The resulting regularly spaced charging steps in the tunneling I-V spectrum are then described by the "orthodox theory" of single electron tunneling [4–7]. Within this theory, the two tunnel junctions formed by insulating gaps between the nanoparticle and the macroscopic electrodes are modeled after the circuit shown in Figure 1(b). The capacitors in this model are ordinary circuit elements, but the resistors pass charge only in discrete increments and are determined by the tunneling rate for a definite, integer charge-state of the nanoparticle.

The orthodox theory has been quite successful at describing the charging behaviour of larger metal particles. However, for very small particles the spacing of energy levels in the cluster can become comparable to the charging energy (and larger than $k_{\mathrm{B}}T$), thereby complicating the spectra. For such cases, the tunneling spectra should show features related to the density of states of the particular cluster or nanocrystal under study, embedded within the Coulomb staircase. However, the extraction of the density of states of the nanocrystal from such tunneling I-V spectra is an open question in current research [7].

In the present work, 29k nanocrystals have been imaged and spectroscopically analyzed under vacuum using STM and STS at 300 K, 77 K and 8 K on Au(111) and graphite substrates. The imaging gives some insight into interactions between the nanocrystals and the substrate, as well as between the nanocrystals themselves. Low-temperature I-V spectra presented here show multiple Coulomb charging features for isolated nanocrystals, and even for those within nanocrystal islands. At room temperature, the Coulomb staircase is less obvious, but appears to be present in some of the data. The thiol electronic structure does not appear to distort the I-V spectra at the energies of interest here, since alkane thiols have a large energy gap and no localized states at low tunnel voltages [29]. Spectra were modeled using the orthodox theory of single-electron tunneling in order to extract the charging energy and other model parameters. Finally, fine structure observed between charging steps in the I-V spectra is attributed to the quantization of energy levels within the nanocrystal.

The remainder of the text covers the experimental conditions, STM imaging results, and tunneling spectra, concentrating separately on spectroscopic features due to Coulomb charging and the quantization of levels.

2 Experimental

Au nanocrystals, each with a mass of ∼29k and a passivating layer of dodecanethiol, were prepared [13] and purified [10] via wet chemical methods that have been described previously. Mass spectrometry indicated a standard deviation of less than 2000 amu in the nanocrystal core mass, which corresponds to at most 10 gold atoms. This leads to an estimate of 147±10 Au atoms in the core, corresponding to a diameter of 1.68±0.04 nm assuming bulk density and a spherical core [21]. The nearest-neighbour distance in a body-centered cubic superlattice of these nanocrystals has been measured to be 3.15±0.02 nm using powder XRD [21].

Substrates for the tunneling experiments were either highly oriented pyrolytic graphite (HOPG) or atomically flat Au(111) on mica [30]. Nanocrystals were pipetted onto the substrates in submonolayer quantities from a solution of nanocrystals dissolved in toluene and allowed to dry slowly at room temperature. Room temperature images and tunneling spectra were acquired using a scanning tunneling microscope mounted inside an ultrahigh vacuum system [31]. The 8 K measurements used a newly developed ultrahigh vacuum STM [32], and 77 K measurements were performed in a low vacuum instrument described previously [33]. Freshly deposited nanocrystal samples were placed on each microscope without further surface preparation or heating. STM imaging was done at high tunnel gap impedance (1–100 GΩ) to minimize tip interactions with the sample.

3 Imaging

3.1 Results

Figure 2 shows a room temperature STM topograph of Au nanocrystal islands on HOPG. The fractional surface

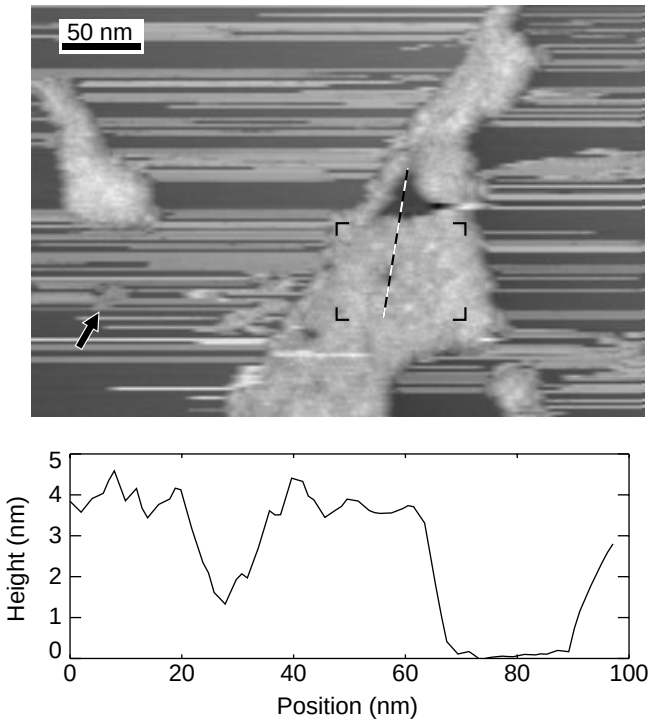

Fig. 2. Top: STM topograph of gold nanocrystal islands on HOPG (tunnel current 10 pA, substrate-tip voltage −1.0 V) for a deposition of ∼ 0.05 ML. The larger island has nucleated at a 1 nm cleavage step, the others on a flat terrace. Streaks are due to the motion of nanocrystals across the HOPG surface. The framed area corresponds to the high resolution image of Figure 3. Bottom: Profile of surface height across the line segment marked in the image. The lowest region of the profile corresponds to the HOPG surface. The island height and the depth of the defect in the profile indicate that the island is 2 ML high. A small 1-ML island appears in the lower left quadrant of the image (arrow).

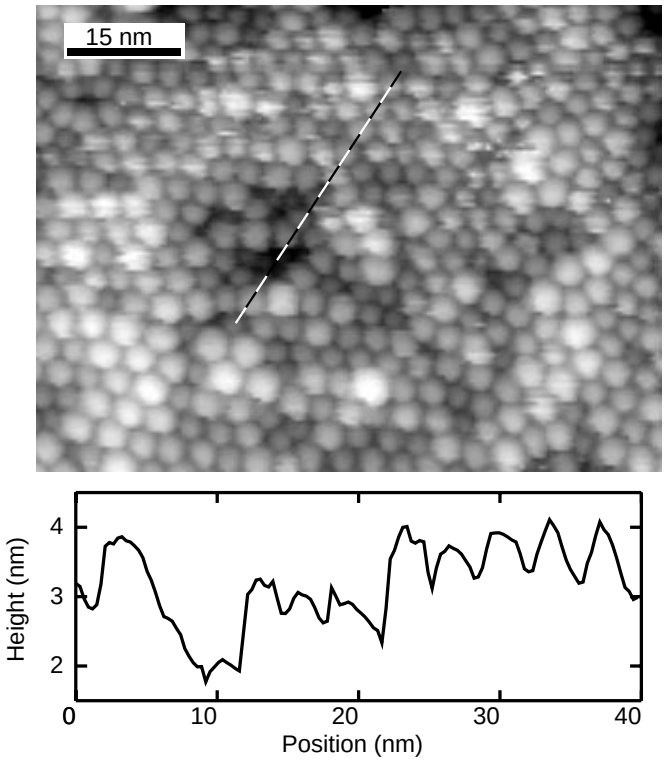

Fig. 3. Top: STM topograph over the framed area shown in Figure 2, under the same tunneling conditions. Local ordering of the nanocrystals is apparent, though the periodicity varies by up to 20%. Variations may be due to different packing of the nanocrystals and their alkane thiol "bundles," disorder in the underlayer, and defects in the nanocrystal superlattice. Bottom: Height profile along the line marked in the image. The zero level corresponds to the HOPG surface, as determined from Figure 2.

coverage of nanocrystals is approximately 0.05 monolayers (ML), where one ML is defined as the density of a close-packed layer of 3.15 nm diameter hard spheres (1.16×10^{13} nanocrystals/cm^2). The larger of the two islands has nucleated at a 1.2 nm high cleavage step while the smaller has nucleated on a terrace. Larger images show a similar trend: nanocrystals are found in isolated islands on atomically flat terraces, or decorating the lower side of a cleavage step, with a few very large islands also found along these steps. For this coverage, the mean island separation was 200 nm. The large island in Figure 2 is 3.8 ± 0.5 nm high, as determined from an area average over the lower half of the island. Other islands on the surface are of similar height. A height profile that crosses both a region of bare HOPG and a defect in the island is also shown in Figure 2. The depth of the defect (∼ 1/2 the island height) suggests that the island consists of more than one nanocrystal layer. Finally, it can be seen that over much of the HOPG surface lying outside of the islands, distinct streaks (typically 2 nm high) extend along the fast scan direction of the STM raster image.

The packing structure of nanocrystals within an island is revealed in Figure 3, which is an STM image acquired over the area shown framed in Figure 2. Local hexagonal order is apparent in the image, with a mean nearest-neighbour distance of 3.8 nm, varying by ±10% from one region to another in Figure 3. The height of the top layer of nanocrystals varies by ±15% across the island, and there appears to be a correlation between the high regions and those of large nearest-neighbour spacing.

3.2 Discussion

Several qualitative conclusions can be made from the results presented in Figure 2. First, the nanocrystals are quite mobile on HOPG. This is a necessary requirement for the formation of well-separated islands. The mean diffusion length must be comparable to the separation between nanocrystal structures. Recent theoretical results [34] attribute the high mobility to a weak alkyl-surface interaction. Of course, the actual deposition process is quite complex since the aggregation and mobility of the nanocrystals may be influenced by the toluene solvent. It is possible that the solvent plays a dominant role in the

formation of the nanocrystal structures, *i.e.* the islands could nucleate in the bulk of the fluid or at the air/solvent interface before settling on the substrate. However, the observation of nanocrystals decorating cleavage steps on the graphite surface supports the notion that surface mobility of individual nanocrystals determines much of the resulting island structure.

From other images and accompanying spectra, we conclude that the streaking seen in Figure 2 is due to mobile nanocrystals that have broken free of the islands. Spectra acquired over the clean surface are metallic in nature, whereas those taken over a streak show features characteristic of a nanocrystal located between the tip and substrate. Height data are consistent with a 1.7 nm nanocrystal core a few Å from the surface [34], whose layer of passivating molecules adds little to the topographic displacement during imaging [29]. At an imaging temperature of 8 K the streaks are fewer in number, but still occur. Therefore, most of these events are initiated by interaction with the STM tip as opposed to simple thermal detachment from the islands (note also how the streaks tend to terminate on a nanocrystal island).

The larger island in Figure 2 has an average height of approximately 3.8 nm. We believe that this cannot correspond to a single layer of nanocrystals for a number of reasons. First, the measured heights of individual, immobilized 29000 amu nanocrystals have been measured to be about 2.5 nm [35]. This is significantly smaller than the average height of the island, indicating the presence of more than one monolayer of material. Further evidence can be found by considering the depth of the depression shown in the images and profiles of Figures 2 and 3. The depression is about 2 nm deep, corresponding to $\sim 1/2$ the island height, and in the profile of Figure 3 the top of a nanocrysal can be just seen at the bottom of the depression. Also, the topography of the island varies much more than one would expect from a close-packed monolayer of nanocrystals on HOPG [36]. Considering these height variations and the mean heights of the islands, we conclude that they consist of poorly ordered bilayers. A few very small, monolayer-high islands can be found on the surface (see Fig. 2, lower left), though they appear to be far less stable than the bilayer islands.

Figure 3 appears to show some polydispersity in this bilayer island, with the nanocrystals tending to segregate and order according to their apparent size. The variation of nearest-neighbour spacing in the island is larger than can be accounted for by changes in the nanocrystal core size, since careful mass spectroscopic analysis of the sample indicates variations in mass of 3.4%, implying only 1.1% deviations in core diameter [18]. One possible explanation is that the image does not reflect the true nanocrystal spacing in the island. This could be because of direct tip interaction with nanocrystals in the island, or because local changes in the current-voltage characteristics change the apparent height of some areas. Neither mechanism can be excluded, but even if the STM image does not map the true height, the nanocrystal packing is clearly inhomogeneous. It is also difficult to construct a mechanism by which the periodicity of an entire region in the image could differ substantially from the actual periodicity in that region. Isolated high spots often appear very wide in the STM due to wave function spreading and the finite size of the tip, but a periodic structure will simply decrease in amplitude as a result of these effects. Therefore, we believe that the observed variations in periodicity are real.

The fluctuations in both periodicity and height are related to imperfect packing of nanocrystals in the top and underlying layer. The interaction between nanocrystals is dominated by the hydrocarbon interaction energy [34]. The 3-dimensional (3D) structure is driven largely by this interaction and the interdigitation of alkane thiol "bundles" on the facets of each nanocrystal core [34,37]. Thin films and powders of these nanocrystals have been found by small angle XRD [10] and by molecular dynamics simulations [34] to form body-centered cubic (bcc) superlattices. The small angle XRD data show that the films grow oriented along the [110] direction. Conversely, STM micrographs such as Figure 3 show a preferential hexagonal local ordering of the nanocrystals at low coverage. It appears that the nanocrystals prefer to be nearly close packed in monolayer films [36], but as more layers are added, the orientation of the nanocrystals and the consequent interdigitation of their passivation layers must determine the packing, making bcc the energetically favourable structure for the 3D superlattice. The islands shown in Figures 2 and 3 may be at a transitional stage where the orientational ordering of nanocrystals is determined partially by the substrate and partially by the bulk orientation required to achieve bcc packing. Any nonuniform orientation of nanocrystals in the island leads to inconsistent packing and interdigitation and thus variable nearest-neighbour spacing.

4 Spectroscopy: Coulomb charging

4.1 Results

Room temperature spectroscopy has been performed on the multilayer island of Figure 3, as shown in Figure 4. *I-V* spectra were taken at the points labeled in the image at the top of Figure 4, using the method of interrupted feedback [38]. The positions of spectra 1 and 2 were chosen to lie between nanocrystals in the image, while spectra 3 and 4 lie directly over nanocrystal maxima. Two spectra from "clean" regions of the HOPG substrate (*i.e.* regions with no streaks) are also shown at the bottom of Figure 4 for comparison. The nanocrystal *I-V* spectra are clearly not Ohmic, showing a gap with zero slope about the zero of sample bias, while the HOPG spectra are characteristic of tunneling between macroscopic metal electrodes, showing a finite slope at zero bias. Dashed lines in Figure 4 show *I-V* curves acquired after pushing the STM tip 0.1 nm closer to the sample. These data confirm that the gap remains in the nanocrystal spectra even when the current sensitivity is increased by decreasing the tip-sample distance.

Current *versus* voltage spectra with substantially more pronounced current steps have been acquired at a temperature of 77 K. Figure 5 presents four spectra from a Au(111) sample prepared with a very low coverage of nanocrystals (< 0.01 ML). Nanocrystals were observed at grain boundaries on this sample, but the spectra shown did not correlate with any nanocrystals in the images. Consequently, we believe that this nanocrystal was adsorbed to the end of the gold STM tip. Six steps in the current, evenly spaced at 327±2 mV increments, are seen in each spectrum. A fit to curve (d) is shown as a dashed line in the figure.

4.2 Discussion

The distinct steps and zero bias gap observed in the low-temperature spectra of Figure 5 are clear indications of single-electron charging of the nanocrystal [4–7]. This Coulomb blockade is a well-known manifestation of the finite energy required to change the charge on a small electrode by a single elementary charge e. The Coulomb staircase spectra presented in Figure 5 are among the few for which the particle size is separately known, though the adsorption geometry on the STM tip is still uncertain. For the present case of passivated nanocrystals, the observation of equally spaced charging steps is particularly important, because it indicates that the effective capacitance C remains constant with charge, as should be the case for itinerant charge distributed over the outer surface of a metallic core [39]. Electrons localized in the thiol adsorbates (or at specific sites in a *non*metallic core) would be very unlikely to produce equivalent charging energies over the ±3-electron charge range measured in this work. Consequently, we view the passivation layer as an insulator that changes the nature of the evanescent states in the tunnel barrier without locally binding any charge. Furthermore, no indications of thermally activated transport (*e.g.* through localized trapping states) have been apparent in our measurements from 8 K to 300 K. Note that the evanescent states may still affect the distribution of charge on the nanocrystal/thiol complex, in a manner analogous to the "metal-induced gap states" that create the dipole layer at a metal/semiconductor interface [40]. However, the equally-spaced charging steps show that any charge in the thiol layer must be delocalized, with successive electrons (holes) occupying orbitals of similar spatial extent. Recent calculations on smaller passivated nanocrystals support these conclusions [41].

In order to further quantify the charging effects observed at 77 K, the analytical expressions of Amman *et al.* [6] have been used to model the spectra of Figure 5. The multiparameter least-squares fit is based on the double tunnel junction model depicted in Figure 1(b). In this model, the capacitances C_1 and C_2 determine the energy required to charge the nanocrystal and the division of voltage across the junctions, while the resistance parameters determine the tunnel rates. The dashed line in Figure 5 represents the best model fit of curve (d), using the parameters $C_1 = 0.59$ aF, $C_2 = 0.48$ aF, $R_1 = 3$ MΩ, $R_2 = 3.0$ GΩ, $Q_0 = -0.19e$, $T_{\rm eff} = 83$ K (Q_0 is the quiescent charge on the nanocrystal, $T_{\rm eff}$ the effective temperature). The fits typically returned an unreasonably small value for R_1, but the quality of the fit became very insensitive to this parameter below a threshold value (as found also by others [42]). Analysis of the mean-square error for the fit *versus* R_1 gave a threshold value of approximately 3 MΩ, above which the fitting error increased rapidly.

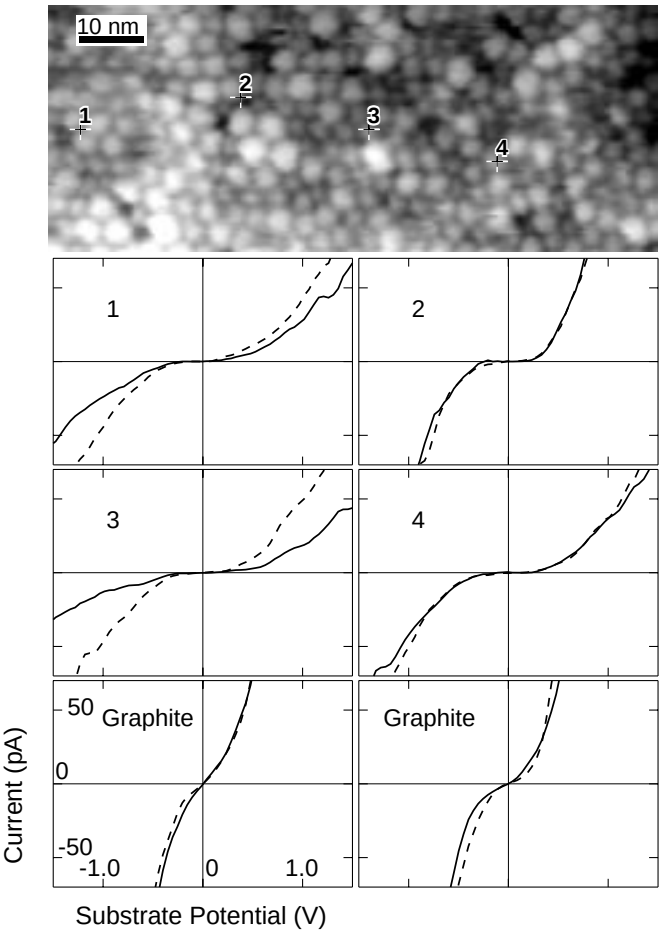

Fig. 4. Room temperature I-V spectra taken over the island shown in Figures 2 and 3 at positions marked in the simultaneously acquired image at top (servo: tunnel current 10 pA, substrate-tip voltage −0.75 V). Spectra 1-4 show a distinct gap around zero tunnel voltage, for positions that lie either between nanocrystals (1,2) or over nanocrystals (3,4). This is the Coulomb blockade. Dashed lines show spectra taken with the tunnel gap reduced by 0.1 nm, showing that the gap remains. For comparison, two I-V spectra taken over the bare graphite surface are displayed at the bottom to show the finite slope at zero tunnel bias. Note that spectra 3 and 4 appear to show steps in the current as well.

The spectroscopic results presented here are analogous to gas phase electron affinity and ionization potential measurements of metal clusters. In gas phase measurements, stripping of electrons is easily achieved whereas experimental measurements of the electron affinity have only succeeded for the removal of a single excess electron [43]. With STS measurements, however, both positive and

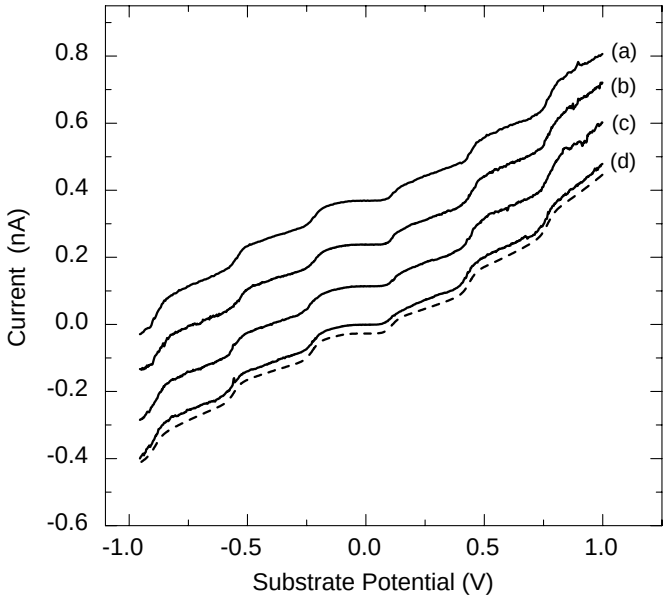

Fig. 5. Successive 77 K spectra (a)-(d) of what is believed to be a single nanocrystal adsorbed on the STM tip (servo: 0.5 nA, 1.0 V). Six reproducible steps are apparent in the series of spectra, with a mean step spacing of 327 mV. This is the Coulomb staircase, where each step occurs at a voltage necessary to change the average charge on the nanocrystal by one electron. The dashed line is a fit of the orthodox model to spectrum (d).

negative charge states can be obtained for multiple excess charges. This is a consequence of the different electrostatic environment for the metal cluster, which includes thiol adsorbates and the proximity of two conducting electrodes. The data in Figure 5 show that the nanocrystals remain stable as they are charged reversibly up to at least the third positive or negative charge state. Results from the fits can be used to obtain the charge addition energy of the nanocrystal by accounting for the voltage division between the two junctions [25], *i.e.* $E_{\rm step} = V_{\rm step} \times eC_1/(C_1 + C_2)$ for $R_2 >> R_1$. An experimental charging energy of $\Delta E_{\rm c}$=167 meV was determined from fits to the four spectra shown in Figure 5.

Gas phase measurements (isolated clusters) are typically compared to the droplet (conducting sphere) model [44], which predicts that transitions between charge states are evenly spaced in energy by e^2/r, the classical Coulomb charging energy for a conducting sphere of radius r. The regular spacing of ionization energies and electron affinities indicates that the distribution of charge on the cluster is nearly classical, and that any discrete quantum levels must be spaced in energy much more closely than the Coulomb energy. For electron transport in mesoscopic devices, a comparable picture has been called the "constant interaction" model [7,45]. In this model the many-electron correlations are treated as a classical Coulomb charging energy ΔE_c that can be separated from the one-electron spectrum of energy states. As for the droplet model, evenly spaced charging features in the tunneling spectra (obtained by adding or removing electrons from the nanocrystal) imply that the charging can be treated classically and that the energy level spacing is negligible compared to the charging energy.

Considering the low-temperature observation of a Coulomb staircase, it is clear that charging effects are important for the 29k Au nanocrystals. In fact, the charging energy measured at 77 K is much greater than $k_{\rm B}T$ even at room temperature, so that for a similar experimental geometry the energy cost of transferring an electron to the nanocrystal should be expected to affect room temperature spectra also. In Figure 4, the zero bias gap seen in spectra acquired over the multilayer island (1–4) is undoubtedly due to the Coulomb blockade. Note that the magnitude of the room temperature blockade region is similar to that at 77 K, even though the geometry is somewhat different than for the single nanocrystal discussed above. The observation of a similar Coulomb gap at positions both between (spectra 1 and 2 in Figure 4) and over (spectra 3 and 4) nanocrystal maxima is consistent with a picture in which excess charge resides only on the nanocrystal core.

The Coulomb staircase is more difficult to observe at elevated temperature than the Coulomb blockade. Nevertheless, recent tunneling spectroscopy results [24,46] have shown that multiple charging levels could be discerned even at room temperature for single nanocrystals of a size similar to those studied in this work. Multiple charge states $(-5 \ldots + 4)$ have also been detected at 300 K via electrochemical measurements on large ensembles of 29k nanocrystals [19]. Close examination of spectrum 3 in Figure 4 shows that even in this superlattice environment, a faint Coulomb staircase can be observed. Since the step shape is affected by the tunneling parameters, it may be possible to find a regime where the Coulomb staircase is more easily visible in room temperature tunneling to such multilayer islands.

5 Spectroscopy: Quantization of levels

5.1 Results

In addition to charging steps, *I-V* spectra acquired over the 29k nanocrystals at 77 K typically show smaller features in the regions between charging steps. These features become more apparent in plots of $\mathrm{d}I/\mathrm{d}V$ *versus* V, as shown by the thick solid line in Figure 6, which is the numerical derivative of curve (d) from Figure 5. The thin solid line in this figure is the same spectrum, but offset vertically and shifted by 327 mV, corresponding to the charging energy $\Delta E_{\rm c}$ = 167 meV. Vertical lines between the two curves show that some of the fine structure on the negative bias part of the spectrum repeats from one charge state to the next.

In order to verify that such fine structure is not simply tunneling noise, spectra were acquired in sequential forward and reverse voltage sweeps at temperatures of 77 K and 8 K. The 77 K $\mathrm{d}I/\mathrm{d}V$ spectra shown in Figure 7 were obtained in a single forward/reverse cycle for a 29k nanocrystal adsorbed to the STM tip. The 8 K spectra

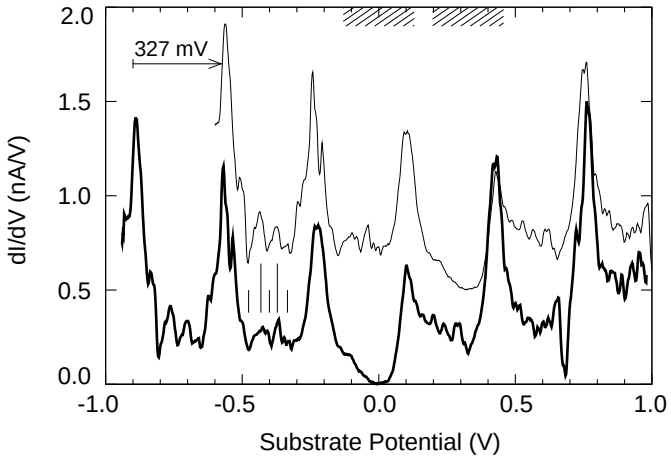

Fig. 6. Thick solid line: Numerical derivative of spectrum (d) from Figure 5 using an effective filter width of 27 mV FWHM (approximately Gaussian; equivalent to 14 meV energy width). Thin solid line: The spectrum shifted by one charging step and offset vertically for display. Using model parameters given in the text, the 327 mV shift is due to a charging energy of 167 meV. Long and short vertical lines near -0.4 V mark similar features in the original and shifted spectra. The repetition of spectral features on successive charging steps is expected for those features that are due to quantization of the nanocrystal energy levels. Within the hatched ranges, comparison of the spectra is complicated by the Coulomb blockade.

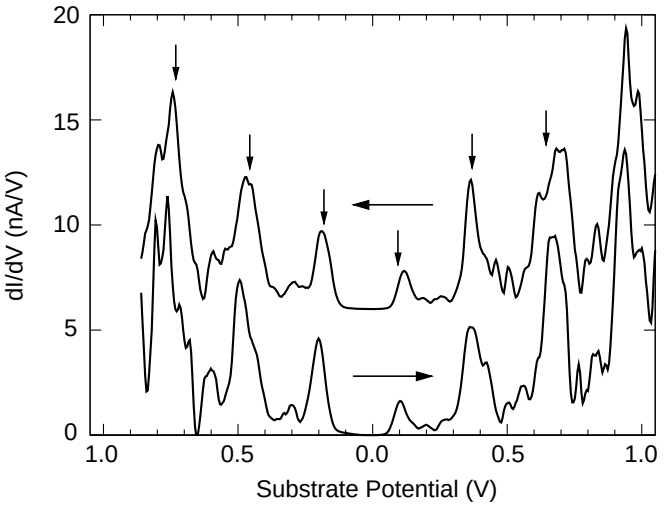

Fig. 7. Derivative spectra for forward (→) and reverse (←) voltage sweeps (numerical derivatives, filter width 27 mV), acquired at 77 K from a nanocrystal believed to be adsorbed on the STM tip (servo setpoint: 1 nA, 0.5 V; data is from a different experiment than that shown in the previous figure). The reverse spectrum has been offset vertically. Spectra shown are from a single forward/reverse acquisition cycle, where the tip-sample tunnel gap was decreased 0.1 nm from the gap determined by the servo setpoint. Downward arrows mark the charging peaks. Most of the fine structure between charging peaks on the forward trace is reproduced on the reverse, and there is some repetition of the fine structure from one charge state to the next, particularly at negative substrate bias.

of Figure 8 were averaged over 20 forward/reverse voltage sweeps while positioned over a multilayer island on HOPG. As a consequence of the signal averaging, transient noise should contribute little to the 8 K spectra. From the figures, it is clear that fine structure on an energy scale much smaller than the charging energy is reproduced in the independent forward and reverse traces, and has even survived the signal averaging. Therefore we conclude that the observed fine structure is characteristic of steady-state tunneling between the tip and nanocrystal. It has been verified that the fine structure peaks are inconsistent with a simple superposition of Coulomb staircases, therefore the most likely source of these features is the quantization of energy levels within the nanocrystal.

5.2 Discussion

Before discussing the origin of the fine structure in the derivative spectra, it is worthwhile to point out again that the environments of the nanocrystals corresponding to the 77 K dI/dV spectra (Figs. 6 and 7) and the 8 K spectra (Fig. 8) are different. Also, the effect of coupling among neighbouring nanocrystals on charging and other spectral features is not yet fully understood. Presumably it is this difference in environment, including a change in the equilibrium configuration of the thiols [34], that causes the charging energies to be quite different for the spectra of Figure 6 and Figure 8. In what follows, the discussion focuses on the case of a single nanocrystal, thus it is most relevant to the spectra shown in Figures 6 and 7. Figure 8

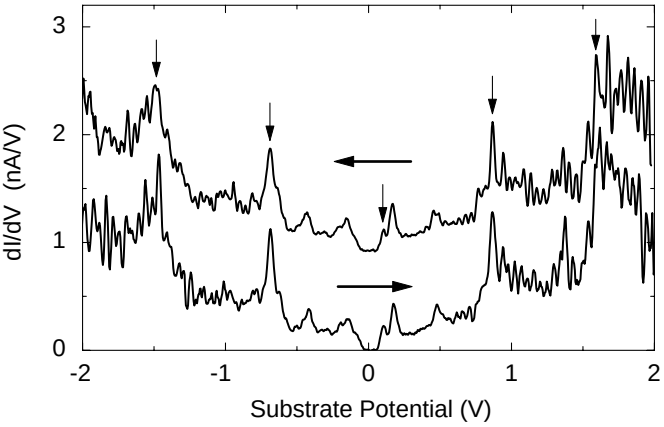

Fig. 8. Forward (→) and reverse (←) dI/dV spectra (numerical derivatives, filter width 27 mV) acquired at 8 K over a nanocrystal within a multilayer island (servo setpoint: 1 nA, -1.5 V). The reverse spectrum has been offset vertically for clarity. The spectra shown are averages of 20 consecutive forward/reverse acquisition cycles, where the tip-sample tunnel gap was decreased 0.1 nm from the gap determined by the servo setpoint. Downward arrows mark charging peaks that fit the orthodox model (parameters: $C_1 = 0.30$ aF, $C_2 = 0.21$ aF, $R_1 = 29$ MΩ, $R_2 = 3.1$ GΩ, $Q_0 = 0.39e$, $T_{\rm eff} = 28$ K). Out to at least ± 1 V, fine structure between charging peaks on the forward trace is largely reproduced on the reverse, indicating that these small features are not due to random noise fluctuations. The fine structure is apparently a consequence of energy level quantization in the nanocrystal.

confirms that the closely spaced features are reproducible for low bias voltages and gives an indication of the very complex structure at higher bias.

For tunneling between macroscopic electrodes the $\mathrm{d}I/\mathrm{d}V$ spectrum is nearly proportional to the one-electron joint density of states, because the transfer of a single electron does not change substantially the Coulomb correlation energy of either electrode, or the occupation of states [38]. Furthermore, if the tip is known to have little structure in the density of states, prominent features can be associated with the sample electronic structure. For the spectra shown in Figures 6–8, the situation is more complex because a single-electron changes the Coulomb energy of the nanocrystal by more than 0.1 eV. However, when changes in electron number are small compared with the total number of conduction electrons, the density of states of the charged nanocrystal is close to that of the neutral cluster, but shifted by the charging energy, and with the level occupancy varying depending on the electron number (the rigid band or constant interaction model [7,45]). For this to hold true, the change in energy of the nanocrystal must also be much less than the barrier heights in order to minimize mixing with tip (or substrate) energy states. Since both assumptions will be satisfied for voltage biases $\lesssim 1$ V, tunneling $\mathrm{d}I/\mathrm{d}V$ spectra in this region should contain structure closely related to the one-electron density of states.

In the nearly free electron (NFE) picture, the density of states of a small metal particle consists of discrete particle-in-a-box energy levels determined by the size of the particle. The nanocrystal density of states at E_F can be estimated from the electronic part of the measured heat capacity for bulk gold [47] as $D(E_\mathrm{F}) = 0.31N/\mathrm{eV}$, where N is the number of atoms. The average energy level spacing is therefore $\bar{\delta}(E_\mathrm{F}) = 6.5\,\mathrm{eV}/N$, assuming spin-degenerate levels. Thus, for a nanocrystal with $N = 145$, $\bar{\delta}(E_\mathrm{F}) = 45$ meV. This estimate does not take into account degeneracies that result from the symmetry of the Au core, which stand to increase the average spacing between levels. It should therefore be considered an approximate lower bound on the energy level spacing. Note that this value is larger than the thermal broadening at 77 K ($3.5k_\mathrm{B}T \sim 23$ meV), so that the quantum levels should be observable, particularly with symmetry-induced degeneracies.

Rösch *et al.* [48] have calculated the eigenstates for a number of structures, including that of an icosahedral gold cluster of 147 atoms. They find that the gap between highest occupied and lowest unoccupied energy levels for the neutral cluster is about 300 meV, with an average level spacing of similar magnitude. They also note that the average level spacing depends strongly on the symmetry of the cluster, with variations up to a factor 3 for icosahedral and octahedral motifs. Considering that icosahedral symmetry is higher than decahedral (hence more level degeneracy), one should expect that the average level spacing in the 29k Au nanocrystal will have an upper bound of ∼300 meV. For low bias voltages, these estimates are consistent with the 8 K experimental data, which have a maximum level spacing of about 150 meV when considering only the largest of the fine structure peaks (energies calculated as described in Sect. 4.2). When considering smaller features, this average is near 50 meV. The 77 K data have average peak spacings of 25-50 meV, which are consistent with the NFE estimate.

It remains to consider in more detail the combined effect of the discrete density of states and finite charging energy on the actual tunneling spectrum. Recent experiments by others have begun to illuminate this issue [49]. In a semiclassical constant interaction picture [7,45], the effect on the tunneling is to create a set of channels corresponding to sequential transport through the nanocrystal with $1, 2, 3, \ldots$ elementary charges resident. The single-electron channel opens at the first charging step, the two-electron channel is added at the second, etc. At the opening of each new channel, the density-of-states structure should repeat itself in the conductance spectrum, though shifted slightly by the change in level occupancy. Since lower-order channels remain open, the spectra will become quite complex after exceeding only 2–3 charging thresholds. Also, at energies where much of the manifold of states becomes accessible, it is possible for the nanocrystal to be left in an excited state after discharge [50]. Figure 8 begins to show very intricate structure for bias voltages above 1 V, possibly due to the wealth of channels and excited states available. This complicated structure could also be related to motions of the charged nanocrystal induced by the high electric field [51].

A search for simplicity in the spectra must begin at low voltage. Within the first two charging steps in Figure 6, there is some repetition of spectral peaks and valleys from one step to the next, most likely due to the quantized one-electron density of states and its charge-shifted replica (compare thick and thin lines in Figure 6). The repetition of features is strongest for negative substrate potential, as indicated by the vertical lines in Figure 6. For these voltages, the electron flow is from substrate to nanocrystal to tip (note that a similar repetition of features can be seen in Figure 7, and in Figure 6 of Ref. [22] for the same sense of electron flow through Pt clusters). The asymmetry in the strength of repetition is most likely a consequence of the asymmetry in the tunneling probability for electron tunneling to or from the nanocrystal. Strong repetition of the density of states features should be expected when the rate-determining step is electron tunneling *from* the nanocrystal. In this case, electron states near the quasi-Fermi-level in the nanocrystal have the highest tunneling probability, independent of the charge state. Conversely, if the rate-limiting step is tunneling *to* the nanocrystal, the electrons that contribute most to the current will be those initially near E_F in the negative electrode. These will be injected into successively higher energy states of the nanocrystal as the tunnel voltage is increased. For a given tunnel voltage, the one-electron states sampled will depend strongly on the charge state of the nanocrystal.

Much work remains to be done in the nanocrystal size regime where both the charging energy and the quantization of levels are important. The observation of repeating

features in the spectra confirms some of the simple ideas presented above and indicates possible ways to extract the one-electron density of states from tunneling spectra, even though the deviation from one-electron behaviour is not small. Fine structure characteristics such as sharp dips and faint peak bunches (Fig. 8) may be due to correlation or nonequilibrium effects [50], but the resolution of these issues may require improved methods for immobilizing individual nanocrystals on the surface [35].

6 Conclusion

Scanning tunneling microscopy and spectroscopy results have been presented for thiol-passivated 29k Au nanocrystals adsorbed to Au(111) and graphite surfaces. Experiments were conducted at room temperature and cryogenic temperatures (77 K, 8 K). The nanocrystals were observed to pack in a nearly hexagonal scheme at room temperature and were found to be highly mobile on each surface. Tunnel spectra showed a clear Coulomb blockade at all temperatures and a Coulomb staircase at low temperatures, independent of whether the nanocrystals were isolated or within an island (although the charging energy varied with environment). In some instances, a faint staircase structure was also apparent for these nanocrystals at room temperature. The regular spacing of charging steps in the Coulomb staircase spectra, up to ± 3 electrons, suggests that changes in the Coulomb correlation energy in these 1.7 nm nanocrystals can be treated as a classical charging energy for a conducting particle, separate from the much smaller energy intervals in the one-electron density of states. At low temperatures, the quantized density-of-states fine structure between charging steps was resolved, confirming that the energy-level spacing is still much less than the charging energy for this size nanocrystal. The repetition of some of of these features from one charge step to the next also confirms the validity of the approximations in the constant interaction model for this system.

We thank U. Landman and M. Shafigullin for useful discussions. This work was supported in part by grants from the National Science Foundation (DMR-9632780 and CHE-9700562) and from the Office of Naval Research (N00014-93-1-0475).

References

1. P.L. Freund, M. Spiro, J. Phys. Chem. **89**, 1074 (1985).
2. A. Henglein, B.G. Ershov, M. Malow, J. Phys. Chem. **99**, 14129 (1995).
3. S. Fafard, Photonics Spectra **31**, 160 (1997).
4. D.V. Averin, K.K. Likharev, in *Mesoscopic Phenomena in Solids*, edited by B.L. Altshuler, P.A. Lee, R.A. Webb (Elsevier, Amsterdam, 1991), p. 169.
5. D.V. Averin, K.K. Likharev, J. Low Temp. Phys. **62**, 345 (1986).
6. M. Amman *et al.*, Phys. Rev. B **43**, 1146 (1991).
7. L.P. Kouwenhoven *et al.*, in *Mesoscopic Electron Transport*, edited by L.L. Sohn, L.P. Kouwenhoven, G. Schön (Kluwer Academic Publishers, Dordrecht, 1997), pp. 105–214, for a recent review.
8. C.L. Cleveland *et al.*, Phys. Rev. Lett. **79**, 1873 (1997).
9. M.M. Alvarez *et al.*, J. Phys. Chem. **101**, 3706 (1997).
10. R.L. Whetten *et al.*, Adv. Mater. **5**, 428 (1996).
11. M. Brust *et al.*, J. Chem. Soc. Chem. Commun. **7**, 801 (1994).
12. M.J. Hostetler *et al.*, Langmuir **14**, 17 (1998).
13. S. Murthy *et al.*, Mat. Lett. **30**, 321 (1997), for preparation of silver nanocrystals. Gold nanocrystals were prepared via a similar synthetic route. The reaction was carried out under ambient conditions using 30 ml of 30 mM $HAuCl_4 \cdot 3H_2O$ in ethanol, 0.20 ml of dodecanethiol and 25 ml of 0.40 M $NaBH_4$, also in ethanol.
14. C. Collier *et al.*, Science **277**, 1978 (1997).
15. J. Dubois *et al.*, Europhys. Lett. **33**, 279 (1996).
16. T.S. Ahmadi *et al.*, Science **272**, 1924 (1996).
17. J. Petrovski, Z.L. Wang, T.C. Green, M.A. El-Sayed, J. Phys. Chem. **102**, 3316 (1998).
18. I. Vezmar *et al.*, Z. Phys. D **40**, 147 (1997).
19. R.S. Ingram *et al.*, J. Amer. Chem. Soc. **119**, 9279 (1997).
20. S. Chen *et al.*, Science **280**, 2098 (1998).
21. T.G. Schaaff *et al.*, Ph.D. Thesis, Georgia Institute of Technology, 1998.
22. J.G.A. DuBois, J.W. Gerritsen, H. van Kempen, G. Schmid, in *Proceedings of the International Symposium on the Science and Technology of Atomically Engineered Materials*, edited by P. Jena, S. Khanna, B. Rao (World Scientific, New Jersey, 1996), pp. 553–562.
23. M. Dorogi *et al.*, Phys. Rev. B **52**, 9071 (1995).
24. R.P. Andres *et al.*, Science **272**, 1323 (1996).
25. D.C. Ralph, C.T. Black, M. Tinkham, Phys. Rev. Lett. **74**, 3241 (1995).
26. D. Klein *et al.*, Appl. Phys. Lett. **68**, 2574 (1996).
27. D.C. Ralph, C.T. Black, M. Tinkham, Phys. Rev. Lett. **78**, 4087 (1997).
28. D. Davidović, M. Tinkham, Appl. Phys. lett. **73**, 3959 (1998).
29. G.E. Poirier, E.D. Pylant, Science **272**, 1145 (1996).
30. J.A. DeRose, T. Thundat, L.A. Nagahara, S.M. Lindsay, Surf. Sci. **256**, 102 (1991).
31. P.E. Quesenberry, P.N. First, Phys. Rev. B **54**, 8218 (1996).
32. L.E. Harrell, P.N. First, Rev. Sci. Instrum. **70**, 125 (1999).
33. G.N. Henderson *et al.*, Rev. Sci. Instrum. **66**, 91 (1995).
34. W.D. Luedtke, U. Landman, J. Phys. Chem. **100**, 13323 (1996).
35. L.E. Harrell *et al.*, submitted to J. Vac. Sci. Technol. B.
36. P.J. Durston, J. Schmidt, R.E. Palmer, J.P. Wilcoxon, Appl. Phys. Lett. **71**, 2940 (1997).
37. Z.L. Wang *et al.*, J. Phys. Chem. B **102**, 3068 (1998).
38. J.A. Stroscio, R.M. Feenstra, in *Scanning Tunneling Microscopy*, edited by J.A. Stroscio, W.J. Kaiser (Academic Press, Toronto, 1993).
39. O.D. Haberlen, S.-C. Chung, N. Rösch, Ber. Bunsenges. Phys. Chem. **98**, 882 (1994).
40. W. Monch, Surf. Sci. **300**, 928 (1994).
41. H. Häkkinen, R.N. Barnett, U. Landman, Phys. Rev. Lett. **82**, 3264 (1999).
42. S. Hong, J. Bielefeld, R.P. Andres, R. Reifenberger, in *Nanowires*, edited by P.A. Serena N. Garcia (Kluwer Academic Publishers, Dordrecht, 1997), pp. 351–371.

43. K.J. Taylor, C.L. Pettiette-Hall, O. Cheshnovsky, R.E. Smalley, J. Chem. Phys. **96**, 3319 (1992).
44. D.M. Wood, Phys. Rev. Lett. **46**, 749 (1981).
45. P.L. McEuen *et al.*, Phys. Rev. B **45**, 11419 (1992).
46. E.S. Soldatov *et al.*, JETP Lett. **64**, 559 (1996).
47. C. Kittel, *Introduction to Solid State Physics* (John Wiley & Sons, Toronto, 1986).
48. O.D. Haberlen, S.-C. Chung, M. Stener, N. Rösch, J. Chem. Phys. **106**, 5189 (1997).
49. D.R. Stewart *et al.*, Science **278**, 1784 (1997).
50. O. Agam *et al.*, Phys. Rev. Lett. **78**, 1956 (1997).
51. L.Y. Gorelik *et al.*, Phys. Rev. Lett. **80**, 4526 (1998).